

# Optimal control for preparing fractional quantum Hall states in optical lattices

Ling-Na Wu,<sup>1</sup> Xikun Li,<sup>2,\*</sup> Nathan Goldman,<sup>3,4,5</sup> and Botao Wang<sup>3,4,†</sup>

<sup>1</sup>*Center for Theoretical Physics and School of Physics and Optoelectronic Engineering,  
Hainan University, Haikou, Hainan 570228, China*

<sup>2</sup>*School of Physics and Optoelectronic Engineering, Anhui University, Hefei, Anhui 230601, China*

<sup>3</sup>*Center for Nonlinear Phenomena and Complex Systems,  
Université Libre de Bruxelles, CP 231, Campus Plaine, 1050 Brussels, Belgium*

<sup>4</sup>*International Solvay Institutes, 1050 Brussels, Belgium*

<sup>5</sup>*Laboratoire Kastler Brossel, Collège de France, CNRS, ENS-Université PSL,  
Sorbonne Université, 11 Place Marcelin Berthelot, 75005 Paris, France*

Preparing fractional quantum Hall (FQH) states represents a key challenge for quantum simulators. While small Laughlin-type states have been realized by manipulating two atoms or two photons, scaling up these settings to larger ensembles stands as an impractical task using existing methods and protocols. In this work, we propose to use optimal-control methods to substantially accelerate the preparation of small Laughlin-type states, and demonstrate that the resulting protocols are also well suited to realize larger FQH states under realistic preparation times. Our schemes are specifically built on the recent optical-lattice experiment [Leonard et al., Nature (2023)], and consist in optimizing very few control parameters: the tunneling amplitudes and linear gradients along the two directions of the lattice. We demonstrate the robustness of our optimal-control schemes against control errors and disorder, and discuss their advantages over existing preparation methods. Our work paves the way to the efficient realization of strongly-correlated topological states in quantum-engineered systems.

## I. INTRODUCTION

The fractional quantum Hall (FQH) effect, a paradigmatic strongly-correlated phenomenon in condensed matter physics, has been a beacon for researchers exploring the interplay between quantum mechanics and topology [1–3]. The FQH states exhibit exotic properties such as topological entanglement and fractional charge excitations [4, 5], which makes the study of FQH states of fundamental interest. Meanwhile, FQH states could also have important impacts on practical applications in quantum information technology [6]. For example, certain FQH states with non-Abelian anyonic excitations could be used for topological quantum computation [7]. It becomes an exciting task to construct a well-controlled device so as to create and manipulate FQH states in a controllable manner.

Advancements in quantum engineered systems, highlighted by the successful creation of artificial gauge fields [8–11], have marked a significant step forward in the pursuit of strongly correlated topological states [12–16]. Recently, Léonard *et al.* successfully realized a Laughlin-type FQH state with two ultracold atoms in a 4-by-4 site optical lattice by using Floquet engineering [17]. Similar FQH states were also explored using rapidly rotating ultracold atoms [18, 19], interacting polaritons [20], and photons in a circuit quantum electrodynamics system [21]. These approaches, while groundbreaking, set the stage for further optimization and exploration of FQH states. In particular, the challenge remains to re-

duce the preparation time to limit undesirable effects like Floquet heating due to periodic driving forces, to enhance the fidelity and robustness of state preparation, especially in the presence of experimental noise and disorder. Most importantly, the need to extend such achievements to larger systems is imperative for advancing quantum simulations and quantum computing.

In this context, the work presented in Ref. [22] employs Bayesian optimization (BO), a machine learning technique, to refine the experimental protocol for realizing the FQH state with ultracold atoms [17]. Different from the experimental protocol based on following the many-body gap across the parameter space, Ref. [22] harnesses the power of BO to search for an optimal ramping protocol. Each parameter is modeled as a piece-wise linear function, which is optimized to reduce the overall experimental costs. Compared to manual ramp design, the ramp protocol optimized by BO is capable of achieving equivalent fidelity (between the final state and the target state) at a speed that is ten times faster, even when considering the disorder present in realistic experimental settings.

In the realm of quantum control, the Bayesian optimization approach, as described in Ref. [22], is not the sole frontier; optimal control theory (OCT) stands as a powerful alternative, with its broad applicability across diverse physical systems, including nuclear magnetic resonance (NMR) [23] and ultracold atoms [24, 25], etc. OCT typically harnesses two principal classes of optimization methodologies: (i) local optimization strategies, with notable examples including Krotov [26], GRAPE [23], CRAB [27], GROUP [28], and GOAT [29]; and (ii) global optimization strategies, exemplified by differential evolution (DE) [30] and covariance matrix adap-

\* xikunli@ahu.edu.cn

† botao.wang@ulb.be

tation evolution strategy (CMA-ES) [31]. While analytic solutions are readily at hand for scenarios where the quantum system's Hilbert space is of low dimension [32–42], high-dimensional quantum systems demand the invocation of numerical optimization techniques. This numerical reliance has made the application of OCT in strongly correlated systems largely uncharted.

In this paper, we leverage OCT to speed up the preparation of FQH states. We achieve this by employing cubic spline functions for the control parameters within the ramp protocol, which are refined using CMA-ES to enhance the fidelity of the system. Our optimized ramp protocol has proven to be efficient, achieving higher fidelity at a faster pace compared to previous results [17, 22]. We also demonstrate its resilience against the impact of disorder and control errors. Moreover, our work not only underscores the successful implementation of these optimization techniques in the existing (Harvard) 4-by-4 lattice with two bosons, but also highlights their scalability to larger system configurations (systems of 8-by-4 lattice sites with four bosons are explicitly addressed in this work).

The paper is organized as follows: Section II describes the theoretical background and the model that forms the basis of our investigation. Section III presents an in-depth analysis of the performance of our optimized protocols within a 4-by-4 lattice, specifically for two particles. This section accentuates the effectiveness of our methods, showcasing not only their better performance but also their resilience in the presence of noise. Building upon the findings for the small system, Section IV extends our discussion to larger system sizes, demonstrating the scalability of our approach and its continued relevance as the complexity of the system increases. Section V wraps up the paper with a summary of the main results.

## II. THEORETICAL BACKGROUND AND MODEL

Considering strongly-interacting bosons moving in a two dimensional square lattice subject to a uniform magnetic flux, the system can be described by the following Harper-Hofstadter-Hubbard (HHH) Hamiltonian [43–45],

$$\begin{aligned} \hat{H}_{\text{HHH}} = & -t_x \sum_{x,y} \left( e^{-i\phi y} \hat{a}_{x+1,y}^\dagger \hat{a}_{x,y} + \text{H.c.} \right) \\ & -t_y \sum_{x,y} \left( \hat{a}_{x,y+1}^\dagger \hat{a}_{x,y} + \text{H.c.} \right) \\ & + \frac{U}{2} \sum_{x,y} \hat{n}_{x,y} (\hat{n}_{x,y} - 1). \end{aligned} \quad (1)$$

Here,  $\hat{a}_{x,y}^\dagger$  and  $\hat{a}_{x,y}$  are the bosonic creation and annihilation operators at lattice site  $(x, y)$ , and  $\hat{n}_{x,y} = \hat{a}_{x,y}^\dagger \hat{a}_{x,y}$  counts the corresponding particle number,  $t_x$  and  $t_y$  denote the strength of the nearest-neighbor tunneling along

the  $x$  and  $y$  direction, respectively;  $U$  is the on-site interaction strength. The Peierls phase factor  $e^{-i\phi y}$  corresponds to a uniform magnetic flux  $\phi = 2\pi\alpha$  per plaquette.

The HHH model is a paradigmatic model of fractional Chern insulators (FCIs), which are lattice analogues of FQH states [46–49]. In the strongly-interacting regime, it has been numerically established that the HHH model hosts a bosonic FCI state akin to the Laughlin state at filling  $\nu = 1/2$  [45, 50–65]. The topologically nontrivial properties can be characterized by e.g. a fractional many-body Chern number  $\nu_{\text{MB}} = 1/2$  [66, 67]. Despite the identification of various preparation schemes [68–80], their experimental realization in optical lattices with ultracold atoms has been challenging.

Only recently, the realization of the  $\nu = 1/2$  FCI state with ultracold atoms was achieved by using two atoms in a strongly-interacting optical lattice [17]. Facilitated by the ability of site-resolved control in a quantum gas microscope, the authors designed an adiabatic-state-preparation scheme. Specifically, two linear gradient potentials were introduced in order to prepare the target FCI state. The corresponding system Hamiltonian reads

$$\hat{H} = \hat{H}_{\text{HHH}} + \Delta_x \sum_{x,y} x \hat{n}_{x,y} + \Delta_y \sum_{x,y} y \hat{n}_{x,y}, \quad (2)$$

with  $\Delta_x$  and  $\Delta_y$  being the potential gradients in the  $x$  and  $y$  directions, respectively. A ramp protocol was employed to adiabatically steer the system from an initial state with two localized particles in a  $4 \times 4$  lattice to the target state. This protocol involved the sequential adjustment of the four control parameters  $\{t_x, t_y, \Delta_x, \Delta_y\}$ . The ramping speed for each control parameter was set to be inversely proportional to the energy gap, a technique aimed at suppressing the system's excitation. Inspired by the high controllability of various system parameters, the protocol presented in Ref. [22] involved the simultaneous adjustment of all four control parameters, following a piece-wise linear function characterized by a set of parameters, which were optimized by using BO.

In this work, we employ the CMA-ES algorithm [31] to do the optimization; see Appendix A for a brief introduction to CMA-ES. The control fields are determined by using a cubic spline function to interpolate between a set of parameters evenly spaced in time. The tuning of these parameters is directed towards increasing the fidelity between the final achieved state  $|\psi_f\rangle$  and the target state  $|\psi_{\text{target}}\rangle$ ,

$$F = |\langle \psi_f | \psi_{\text{target}} \rangle|^2. \quad (3)$$

The fidelity serves as a reliable performance metric, which was also utilized in the experiment [17], where it was assessed by reversing the ramp process and measuring the fraction of the system that returns to its initial state. For the experimental protocol [17], it was measured to be  $F = 43(6)\%$  over a total evolution time of  $T = 100\tau$ , with the tunneling time  $\tau = 4.3(1)$  ms. In Ref. [22], BO identified an optimal ramp with  $F = 94.5\%$

over the same evolution time  $T = 100\tau$ . When the evolution time was curtailed to  $T = 20\tau$  and  $T = 10\tau$ , the fidelity gravitated to 78% and 53%, respectively. In the following, these fidelity values establish the benchmark against which the merits of our proposed schemes are evaluated.

### III. OPTIMIZATION OF THE HARVARD EXPERIMENT

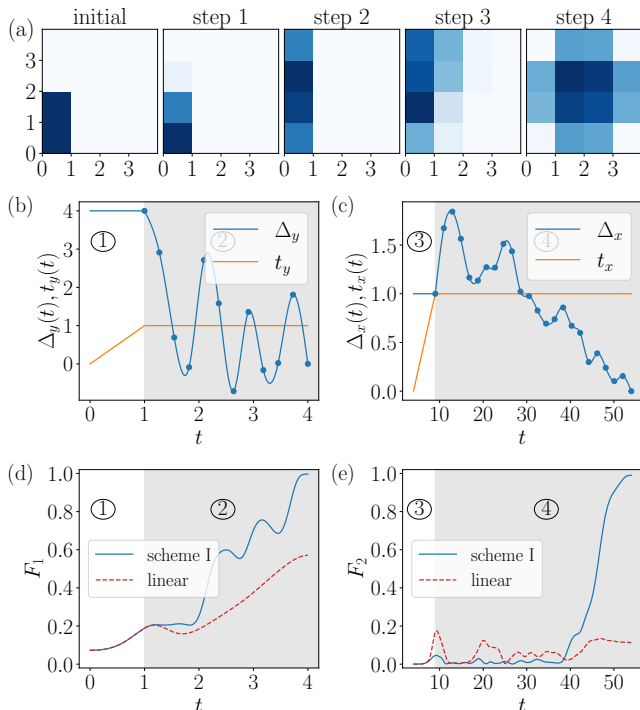


FIG. 1. FQH state preparation for a  $4 \times 4$  lattice with two particles using Scheme I. (a) Particle density distribution during the whole process of state preparation. The first plot shows the particle density at the initial moment, where two localized atoms are on two sites. The following four plots show the particle density of the final state at each step. (b) Linear ramp  $t_y(t)$  in step 1 and optimized control field for tilt  $\Delta_y(t)$  in step 2 (gray shading). (c) Linear ramp  $t_x(t)$  in step 3 and optimized control field for tilt  $\Delta_x(t)$  in step 4 (gray shading). The blue bullets denote the interpolating parameters optimized. (d,e) Evolution of the fidelity between the instantaneous state and the corresponding target states,  $F_i = |\langle \psi_{i,\text{target}} | \psi(t) \rangle|^2$ . A nearly perfect fidelity  $F = 99.0\%$  with the target state in step 4, i.e., the Laughlin-type FQH state, is obtained with a duration  $T_1 + T_2 + T_3 + T_4 = 1\tau + 3\tau + 5\tau + 45\tau = 54\tau$ . Optimization is conducted utilizing the Python package CMA-ES [81]. As a comparison, the linear scheme gives a low fidelity within the same time, as shown by the red dashed line.

In this section, we focus on the system of  $4 \times 4$  lattice with two bosonic particles. We directly simulate the effective Hamiltonian instead of modeling the Floquet sequence as performed in the experiment [17]. The state

preparation begins from an initial state of two localized atoms along the  $y$ -axis, as shown in the first panel of Fig. 1(a). The target state is chosen as the ground state of the Hamiltonian (2) with  $\{t_x = \hbar/\tau, t_y = \hbar/\tau, \Delta_x = 0, \Delta_y = 0\}$ . We set the tunneling amplitudes in the target state,  $\hbar/\tau$ , as the unit of energy, and use the tunneling time  $\tau$  as the unit of time. The flux is kept constant at  $\phi = 2\pi \times 0.26$  and the on-site interaction  $U = 8\hbar/\tau$ , so that the target state is the Laughlin-like state at filling  $\nu = 1/2$  [17]. For a fair comparison with previous work [17, 22], we elect to navigate within an analogous parameter regime:

$$0 \leq t_{x,y} \leq 1.2\hbar/\tau \quad \text{and} \quad -4\hbar/\tau \leq \Delta_{x,y} \leq 4\hbar/\tau. \quad (4)$$

Note that the relatively small range of  $t_{x,y}$  (which corresponds to small driving amplitudes in experiments) could facilitate to reduce Floquet heating caused by excitations to higher bands [17, 22, 82]. In the following, we employ two schemes to speed up the process of state preparation.

#### A. Scheme I: four-step state preparation

We first study a four-step scheme where only one parameter is tuned at each step, like the protocol applied in the experiment [17]. As the benefits from fine-tuning the hopping amplitudes  $t_{x,y}$  are rather modest [22], we shall linearly ramp up hopping amplitudes  $t_{x,y}$  and perform optimization on the tilt potential gradients  $\Delta_{x,y}$ . Choosing the initial and final values of the control fields according to the experimental protocol [17], the state preparation consists of the following four steps:

1. Linearly ramp up  $t_y$  from 0 to  $\hbar/\tau$  over duration  $T_1 = \tau$ , and keep the other three parameters constant:  $t_x = 0$ ,  $\Delta_x = \hbar/\tau$ , and  $\Delta_y = 4\hbar/\tau$ . The final state in this step is the initial state of next step.
2. While keeping  $t_x = 0$ ,  $t_y = \hbar/\tau$ ,  $\Delta_x = \hbar/\tau$  constant, optimize the ramp protocol of  $\Delta_y(t)$  within time  $T_2$  to maximize the fidelity between the evolved state  $|\psi(T_1 + T_2)\rangle$  and the intermediate target state  $|\psi_{1,\text{target}}\rangle$ , which is the ground state of the Hamiltonian (2) with no tilt in  $y$ -direction  $\Delta_y = 0$ .
3. Linearly ramp up  $t_x$  from 0 to  $\hbar/\tau$  over duration  $T_3 = 5\tau$ , and keep the other three parameters constant:  $t_y = \hbar/\tau$ ,  $\Delta_x = \hbar/\tau$ , and  $\Delta_y = 0$ .
4. Keeping the other three constant:  $t_x = t_y = \hbar/\tau$ ,  $\Delta_y = 0$ , optimize the ramp protocol of  $\Delta_x(t)$  within  $T_4$  to maximize the fidelity between the final state and the target FCI state  $|\psi_{2,\text{target}}\rangle$ , which is the ground state of Hamiltonian (2) with tunneling strengths  $t_x = t_y = \hbar/\tau$  and  $\Delta_x = \Delta_y = 0$ .

The resulting density distributions for each step are depicted in Fig. 1(a). One can see that after ramping

down the tilt in  $y$ -direction (step 2), the particles delocalize along this direction. The dispersion across the  $x$ -direction is achieved once the tilt in that direction is similarly diminished (step 4), culminating in a flat density distribution in the bulk [see the last panel of Fig. 1(a)], a hallmark characteristic of the FQH state. Figures 1(b) and (c) show the control fields associated with steps 1-2 and 3-4, respectively. The optimized control fields are distinctly marked with a gray background for ease of identification. The progression of the fidelity, comparing the time evolved state to the target state of step 2 and step 4, is displayed in Figs. 1(d) and (e), respectively. An elevated fidelity level of 99% is achieved within a total time duration of  $T = T_1 + T_2 + T_3 + T_4 = 1\tau + 3\tau + 5\tau + 45\tau = 54\tau$ . We have also used GRAPE to perform the optimization, which gives similar results, as shown in Appendix B. Note that a linear ramping protocol (red dashed lines) yields a comparatively lower fidelity within the same evolution time. Moreover, our results exceed those in Ref. [22], which attained a fidelity of 94.5% at  $T = 100\tau$ .

Figures 2(a,b) show the distribution of weight among the eigenstates of the instantaneous Hamiltonian during the final stage of preparation, which offers a glimpse into the excitation patterns. It is noticeable that minor excitations to the low-energy excited states occur throughout the process. Nonetheless, these excited populations eventually revert to the ground state by the end of the ramp protocol. This observed excitation behavior is starkly distinct from that encountered in adiabatic protocols, where the parameters must be ramped very gradually—a requirement that necessitates a significantly longer evolution time—to ensure that the system remains in the ground state of the instantaneous Hamiltonian throughout the process.

The final stage of the process is the most time-consuming. Figure 3 illustrates how the ultimate fidelity is contingent upon the duration of the last step ( $T_4$ ). As expected, increasing  $T_4$  results in an enhanced fidelity. Notably, the fidelity surpasses 95% once  $T_4$  exceeds  $35\tau$  (corresponding to a total evolution time of  $T = 44\tau$ ).

## B. Scheme II: two-step state preparation

The second scheme involves a two-step process: (i) the tunneling parameter  $t_y$  and tilt  $\Delta_y$  along the  $y$ -axis are optimized simultaneously to prepare the ground state of Hamiltonian (2) with  $t_y = \hbar/\tau$ ,  $\Delta_y = 0$ ,  $t_x = 0$ , and  $\Delta_x = 100\hbar/\tau$  (a large value of  $\Delta_x$  lifts the degeneracy along  $x$ -axis); (ii) the tunneling parameter  $t_x$  and tilt  $\Delta_x$  along the  $x$ -axis are optimized to prepare the ground state of Hamiltonian (1) with  $t_x = t_y = \hbar/\tau$ .

Figures 4(a,b) show the density distributions for the final evolved states of these two steps, and Figs. 4(c,d) showcase the optimized control fields for the two steps, respectively. The evolution of fidelity between the time

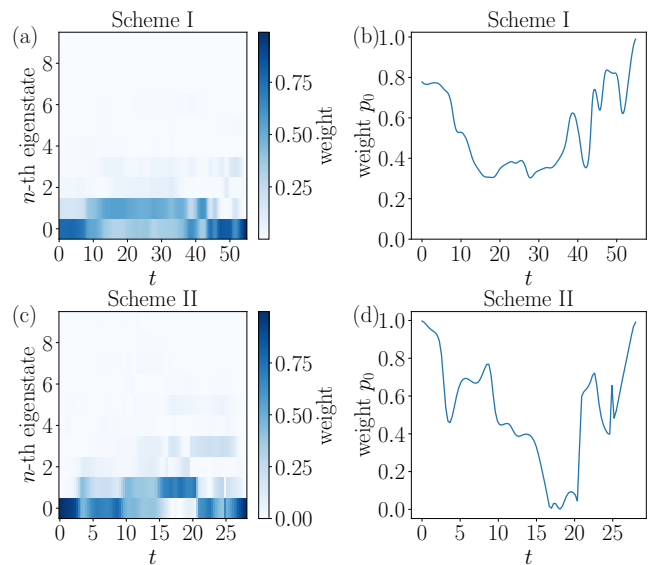


FIG. 2. (a,c) The weight in the lowest few eigenstates during the last step preparation for the two schemes. (b,d) The weight in the instantaneous ground state  $p_0$  during the last step preparation for the two schemes.

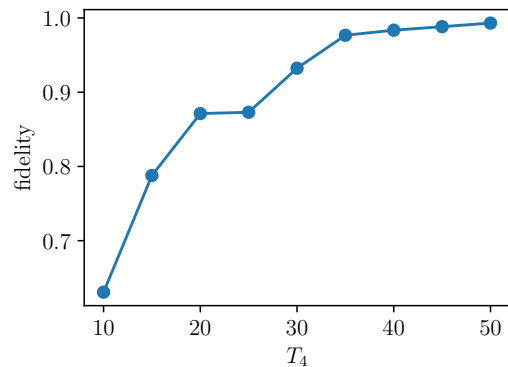


FIG. 3. The final fidelity as a function of the evolution time of step 4 for Scheme I in Section III A.

evolved state and the corresponding target state in each step is depicted in (e,f). Notably, a fidelity of 99.5% is achieved within  $T_1 = 3\tau$  for the first step, while for the second step, a fidelity of 99% is attained within  $T_2 = 28\tau$ . To summarize, a final fidelity of 99% is reached with a total evolution time of  $T = T_1 + T_2 = 31\tau$ . This outcome surpasses the performance of Scheme I. The populations of excited states are illustrated in Figs. 2(c,d), revealing a similar pattern as that observed in Scheme I.

In Fig. 5, we plot the ultimate fidelity as a function of the duration of the last step,  $T_2$ . Impressively, the fidelity climbs above 95% once  $T_2$  surpasses  $20\tau$  (corresponding to a total evolution time of  $T = 23\tau$ ). Meanwhile, we find that using a larger range of  $t_x$  to do the optimization further improves the efficiency. As shown by the orange line in Fig. 5, an enhanced fidelity is observed in scenarios



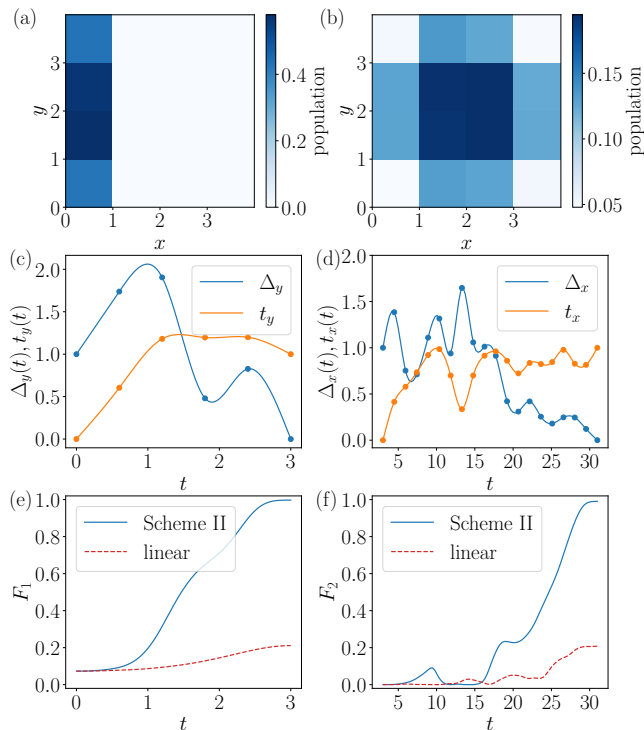


FIG. 4. Particle density distribution of the final state for the first step (a) and the second step (b) of scheme II. (c,d) The optimized control fields for scheme II. (e,f) The evolution of the fidelity between the instantaneous state and the corresponding target state,  $F_i = |\langle \psi_{i,\text{target}} | \psi(t) \rangle|^2$ . The optimized parameters are represented by dots, except for the ends. The optimized parameters are interpolated using a cubic spline to obtain the control field. Optimization is conducted utilizing the Python package CMA-ES [81].

where the limitation on the control field  $t_x$  is relaxed from  $1.2\hbar/\tau$  to  $2\hbar/\tau$ . The detrimental effect of constraints is particularly pronounced for shorter  $T_2$  durations.

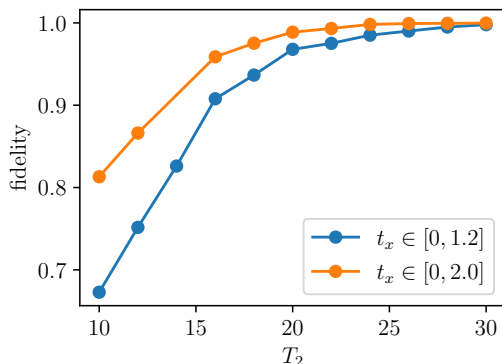


FIG. 5. The final fidelity as a function of the evolution time of the second step for scheme II in Section III B. The blue (orange) data denote the results for the case when the control field  $t_x$  is bounded by  $[0, 1.2]$  ( $[0, 2.0]$ ).

## C. Robustness to noise

### 1. Control error

In experiments, achieving the desired control field with perfect precision is often challenging. To evaluate the resilience of our protocols against potential inaccuracies in the control fields, we subject the optimized control fields to random perturbations. Specifically, the control inaccuracies are modeled as white noise that is added onto the control field. This noise, represented by  $\delta(t)$ , is applied with a frequency of  $f$ . The perturbed control field at time  $n\Delta t$  (where  $n$  is an integer and  $\Delta t = 1/f$ ) is expressed as  $h_x(n\Delta t) = h_x^{\text{Opt}}(n\Delta t) + \delta(n\Delta t)$ . Here,  $h_x^{\text{Opt}}(t)$  signifies the ideal control field, and the noise  $\delta(t)$  is a random variable drawn from a normal distribution with mean  $\mu = 0$  and standard deviation  $\sigma$ . The final perturbed control field at arbitrary time is obtained by interpolating these values using a cubic spline function.

A depiction of the noisy control fields (with noise strength  $\sigma = 0.06\hbar/\tau$  and frequency  $f = 10/\tau$ ) for step 2 of Scheme II is provided in Fig. 6(a). We conduct the time evolution with the perturbed control fields across 50 iterations and determine the average fidelity, which is then plotted as a function of the noise strength  $\sigma$  in Fig. 6(b). Both schemes exhibit obvious robustness against control noise. Notably, Scheme I demonstrates greater robustness compared to Scheme II, a difference we attribute to the reduced number of optimized control fields in Scheme I—only two, as opposed to four in Scheme II.

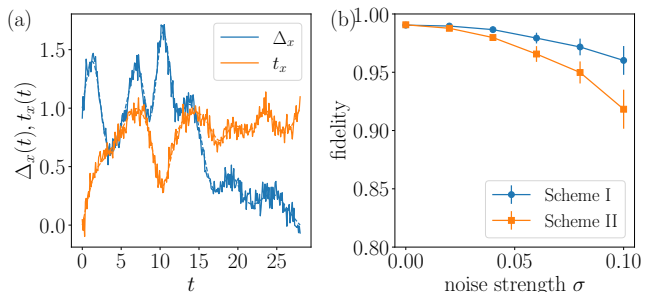


FIG. 6. (a) An example of noisy profile for scheme II at a noise strength of  $\sigma = 0.06\hbar/\tau$  and frequency of  $f = 10/\tau$ . (b) The final fidelity as a function of the profile noise strength with noise frequency  $f = 10/\tau$ . The results are obtained by averaging over 50 runs. The error bars denote one standard deviation. The parameters are  $L_x = L_y = 4$ ,  $N = 2$ ,  $\phi = 2\pi \times 0.26$ ,  $U = 8\hbar/\tau$ .

### 2. Disorder

Considering that disorder is ubiquitous in experiments, here we also evaluate the robustness of the optimized protocols against disorder. We simulate experimental conditions by including static on-site potential shifts in our

simulations. Specifically, each lattice site is impacted by a random offset. The lattice edges experience an additional, uniform offset with the corners receiving twice the impact (caused by the creation of lattice walls via the digital micromirror devices) [17, 22]. The (random and uniform) offsets are modeled to follow a Gaussian distribution, with an average value of 0 and a standard deviation of  $\sigma$ . In Fig. 7, the fidelity of our protocols is shown as a function of the disorder strength  $\sigma$ . The mean fidelity and its standard deviation are obtained by averaging the results over 500 such disorder realizations. One can see that both protocols exhibit a similar level of endurance against the effects of disorder.

Integrating disorder into the optimization process allows for a reduction in its detrimental effects. For optimization in the presence of disorder, we use the average fidelity of 100 disorder realizations as the cost function to reduce fluctuations. The outcomes for Scheme II, represented by green squares, unequivocally demonstrate a diminished influence from disorder. This advantage intensifies as the disorder strength increases.

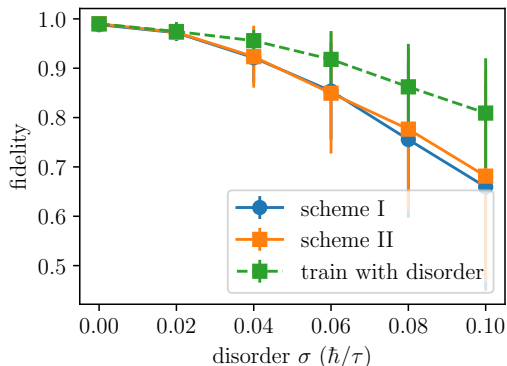


FIG. 7. The fidelity as a function of the disorder strength. The solid lines represent the outcomes when the optimal control field, trained in the absence of disorder, is implemented. In contrast, the dashed lines illustrate the outcomes for scenarios where disorder is considered during the optimization process for scheme II. For this latter scenario, the cost function value is derived from averaging the fidelity across 100 distinct random disorder configurations. The results for both cases are compiled by averaging over 500 instances of disorder. The error bars indicate the standard deviation from the mean. The parameters are  $L_x = L_y = 4$ ,  $N = 2$ ,  $\phi = 2\pi \times 0.26$ ,  $U = 8\hbar/\tau$ .

#### IV. BEYOND TWO PARTICLES

Going beyond two particles, we first focus on a system of  $6 \times 6$  lattice sites with  $N = 3$  particles. To determine the appropriate parameter regime where the system manifests properties of a fractional Chern insulator, we utilize Středa's formula [58, 83–86], which encodes the Hall conductivity  $\sigma_H$  through the static spatial density

distribution. The formula is given by:

$$C_{\text{Str}} = \frac{\partial n_B}{\partial \alpha} = \frac{\sigma_H}{\sigma_0}, \quad (5)$$

where  $\sigma_0 = 1/2\pi$  represents the conductivity quantum. For the  $\nu = 1/2$  Laughlin state,  $C_{\text{Str}} = 1/2$  is expected. This value serves as a benchmark for identifying the correct parameter settings. For each value of flux  $\alpha$  (in unit of  $2\pi$ ), we calculate the system's ground state and determine the density distribution. An illustration of the density distribution for the ground state at  $\alpha = 0.22$  is depicted in Fig. 8(a). The bulk density  $n_B$  within a central disk of radius  $r = 2$  is then extracted to compute  $C_{\text{Str}}$  using Eq. (5). Figure 8(b) displays the bulk density  $n_B$  as a function of  $\alpha$  (in the vicinity of  $\alpha = 0.22$ ). By performing a linear fitting to the data, one can extract the Středa's marker  $C_{\text{Str}}$  from the slope. For instance, from the data in Fig. 8(b),  $C_{\text{Str}}$  is found to be 0.476 for  $\alpha = 0.22$ . Following this method, one can obtain  $C_{\text{Str}}$  as a function of  $\alpha$ , as shown in Fig. 8(c). The expected value of  $C_{\text{Str}} = 1/2$  is marked by the orange dashed line. One can see that for a wide range of  $\alpha$ ,  $C_{\text{Str}}$  is close to the expected value, suggesting the existence of a fractional Chern insulating state. The deviation around  $\alpha = 0.2$  is attributed to the closing of the many-body gap, as shown in Fig. 8(d), signifying a topological phase transition. In the following, we choose the ground state at flux  $\alpha = 0.22$  as our target state.

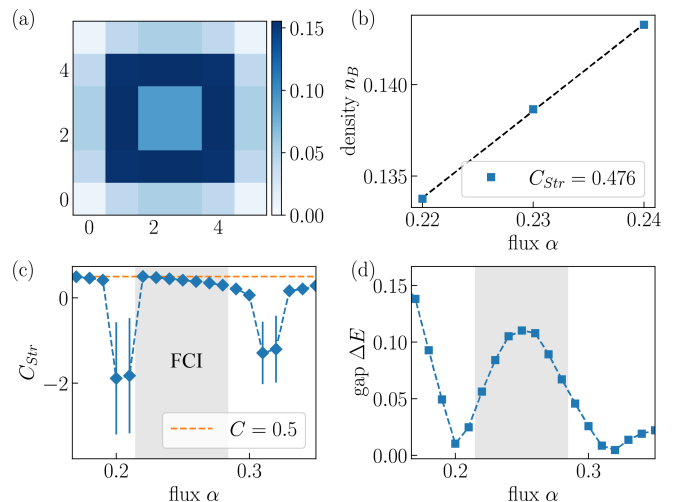


FIG. 8. (a) The spatial density distribution of the ground state at flux  $\alpha = 0.22$  in the  $6 \times 6$  system with  $N = 3$  particles at  $U = 7\hbar/\tau$ . (b) The bulk density  $n_B$  as a function of flux  $\alpha$ . (c) The Středa's marker as a function of flux  $\alpha$ . The expected value of  $C_{\text{Str}} = 1/2$  is marked by the orange dashed line. (d) The many-body gap as a function of flux  $\alpha$ .

The state preparation begins from an initial state of three localized atoms in the  $y$ -axis [see Fig. 9(a)]. By means of CMA-ES strategy, we apply the two-step scheme (scheme II) in the process of state preparation. Figures 9(b,c) show the density distribution for the

evolved states at the end of these two steps, and Figs. 9 (d,e) showcase the optimized control fields for the two steps, respectively. The evolution of fidelity between the evolved state and the corresponding target state is depicted in Figs. 9 (f,g). We find that a fidelity of 99.7% is achieved within  $T_1=5\tau$  for the first step, while for the second step, a fidelity of 96.4% (99.4%) is attained within  $T_2=60\tau$  ( $100\tau$ ). In the end, a fidelity of 96.4% is reached with an overall evolution time of  $T=T_1+T_2=65\tau$ .

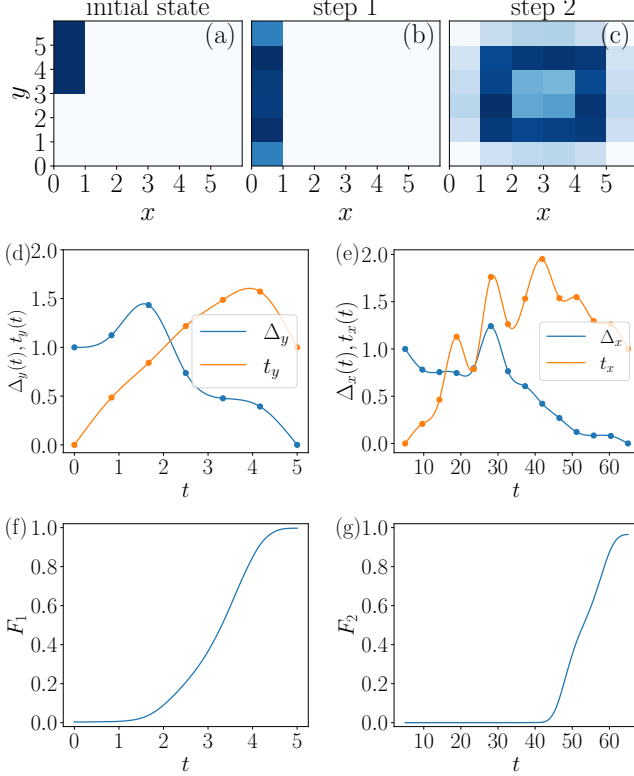


FIG. 9. The on-site population for (a) the initial state, (b) the final state of the first step evolution, (c) the final state of the second step evolution for the two-step scheme. (d,e) The optimized control fields for two-step scheme. (f,g) The evolution of the fidelity between the instantaneous state and the corresponding target state. The parameters optimized are represented by dots, except for the ends. The optimized parameters are interpolated using a cubic spline to obtain the control field. Optimization is conducted utilizing the Python package CMA-ES [81]. The parameters are  $L_x = L_y = 6$ ,  $N = 3$ ,  $\phi = 2\pi \times 0.22$ ,  $U = 7\hbar/\tau$ . A final fidelity of 96.4% is obtained within a total evolution time of  $T=5\tau + 60\tau=65\tau$ .

Finally, we study a system of size  $L_x=4$ ,  $L_y=8$  with  $N=4$  particles. In order to simplify the numerical calculations, we consider the hard-core limit ( $U \rightarrow \infty$ ). Similar analysis based on the many-body gap and Středa's formula suggests that the system exhibits FCI properties [79] at flux  $\alpha \approx 0.3$ . We employ the two-step scheme to speed up the process of state preparation. The state preparation begins from an initial state of four localized atoms in the  $y$ -axis [Fig. 10(a)]. As shown in

Figs. 10(g,h), a final fidelity of 98.1% is obtained within a total evolution time of  $T=6\tau + 80\tau=86\tau$ .

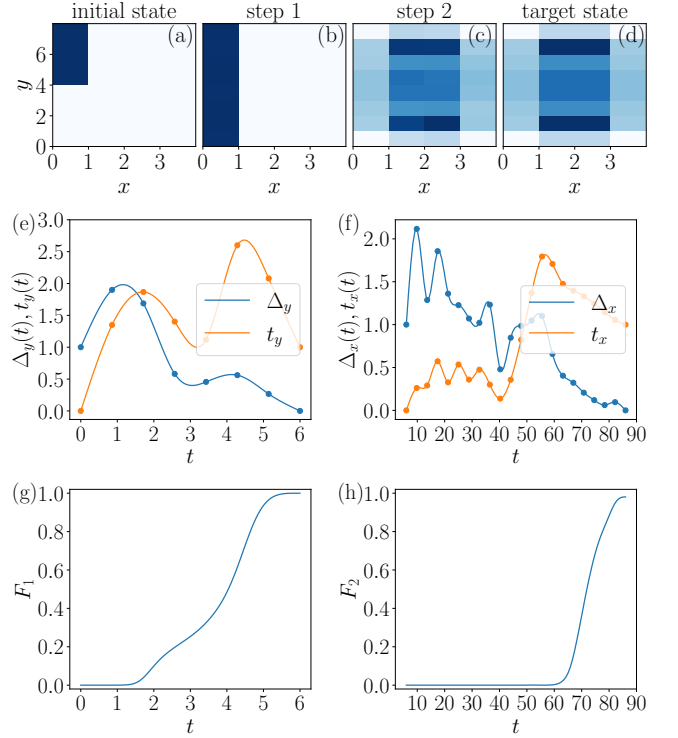


FIG. 10. The on-site population for (a) the initial state, (b) the final state of the first step evolution, (c) the final state of the second step evolution for the two-step scheme, and (d) the target state. (e,f) The optimized control fields for two-step scheme. (g,h) The evolution of the fidelity between the instantaneous state and the corresponding target state. The parameters optimized are represented by dots, except for the ends. The optimized parameters are interpolated using a cubic spline to obtain the control field. Optimization is conducted utilizing the Python package CMA-ES [81]. The parameters are  $L_x = 4$ ,  $L_y = 8$ ,  $N = 4$ ,  $\phi = 2\pi \times 0.3$ , Hard-Core limit. A final fidelity of 98.1% is obtained within a total evolution time of  $T=6\tau + 80\tau=86\tau$ .

## V. CONCLUSION

To sum up, we have discussed how to speed up the preparation of strongly correlated FQH states in optical lattices with ultracold atoms by means of optimal control theory. By employing cubic spline functions for control parameters and refining them using the CMA-ES algorithm, we have investigated two schemes. The first one refines the experimental protocol by optimizing the ramping speed of control parameters. The second scheme introduces a dual-parameter tuning approach, which promises greater efficiency. Both of our optimized ramp protocols have demonstrated better performance over previous methods, achieving higher fidelity

in shorter time, and showcase an impressive ability to withstand the effects of disorder and control errors.

Furthermore, our schemes have proven to be not only effective in the intensively studied 4-by-4 system with two particles, but also readily scalable to more extensive configurations. As an illustration, we have applied our methods to the preparation of FQH states in a 6-by-6 system with three particles and a 4-by-8 system with four particles. In each of these cases, our schemes have delivered good results, i.e. high fidelity ( $\sim 98\%$ ) within realistic preparation time ( $\sim 80\tau$ ). Our work provides new possibility of preparing and manipulating strongly-correlated states in optical lattices with ultracold atoms, and may find broader application in quantum many body systems of increasing complexity.

Considering realistic models that include the periodic driving, it has been shown that the Floquet heating could be suppressed in systems of few particles [77, 87]. In general, it would be interesting to apply our optimal-control protocols in that context to improve the performance of periodically-driven many body system. Considering that optimal control protocols often exploit excited states as intermediate steps (see Fig.2), which is very different

from typical adiabatic preparation schemes, it would be relevant to study efficient optimal preparation sequences that make use of higher bands beyond the tight-binding regime.

## ACKNOWLEDGMENTS

We thank Brice Bakkali-Hassani for his insightful comments on our manuscript. We thank Nathan Dupont, Felix A. Palm and Amit Vashisht for useful discussions. This work is supported by the Hainan Province Science and Technology Talent Innovation Project (Grant No. KJRC2023L05). XL acknowledges the Science Research Project of Anhui Educational Committee (2023AH050073) and the University Synergy Innovation Program of Anhui Province under Grant No. GXXT-2022-039. NG and BW acknowledge the financial support from the ERC (LATIS project), the EOS project CHEQS, the FRS-FNRS Belgium and the Fondation ULB.

- 
- [1] S. M. Girvin, *The Quantum Hall Effect: Novel Excitations And Broken Symmetries* (Springer, Berlin, 2002).
- [2] H. L. Stormer, D. C. Tsui, and A. C. Gossard, The fractional quantum hall effect, *Rev. Mod. Phys.* **71**, S298 (1999).
- [3] B. I. Halperin and J. K. Jain, *Fractional Quantum Hall Effects* (WORLD SCIENTIFIC, 2020).
- [4] X.-G. Wen, Colloquium: Zoo of quantum-topological phases of matter, *Rev. Mod. Phys.* **89**, 041004 (2017).
- [5] D. E. Feldman and B. I. Halperin, Fractional charge and fractional statistics in the quantum hall effects, *Reports on Progress in Physics* **84**, 076501 (2021).
- [6] C. Nayak, S. H. Simon, A. Stern, M. Freedman, and S. Das Sarma, Non-abelian anyons and topological quantum computation, *Rev. Mod. Phys.* **80**, 1083 (2008).
- [7] A. Y. Kitaev, Fault-tolerant quantum computation by anyons, *Annals of Physics* **303**, 2 (2003).
- [8] J. Dalibard, F. Gerbier, G. Juzeliūnas, and P. Öhberg, Colloquium: Artificial gauge potentials for neutral atoms, *Rev. Mod. Phys.* **83**, 1523 (2011).
- [9] N. Goldman, G. Juzeliūnas, P. Öhberg, and I. B. Spielman, Light-induced gauge fields for ultracold atoms, *Rep. Prog. Phys.* **77**, 126401 (2014).
- [10] S.-L. Zhang and Q. Zhou, Manipulating novel quantum phenomena using synthetic gauge fields, *Journal of Physics B: Atomic, Molecular and Optical Physics* **50**, 222001 (2017).
- [11] M. Aidelsburger, S. Nascimbene, and N. Goldman, Artificial gauge fields in materials and engineered systems, *Comptes Rendus Physique* **19**, 394 (2018).
- [12] N. Goldman, J. Budich, and P. Zoller, Topological quantum matter with ultracold gases in optical lattices, *Nat. Phys.* **12**, 639 (2016).
- [13] D.-W. Zhang, Y.-Q. Zhu, Y. X. Zhao, H. Yan, and S.-L. Zhu, Topological quantum matter with cold atoms, *Advances in Physics* **67**, 253 (2018).
- [14] N. R. Cooper, J. Dalibard, and I. B. Spielman, Topological bands for ultracold atoms, *Rev. Mod. Phys.* **91**, 015005 (2019).
- [15] T. Ozawa and H. M. Price, Topological quantum matter in synthetic dimensions, *Nature Reviews Physics* **1**, 349 (2019).
- [16] A. Browaeys and T. Lahaye, Many-body physics with individually controlled Rydberg atoms, *Nature Physics* **16**, 132 (2020).
- [17] J. Léonard, S. Kim, J. Kwan, P. Segura, F. Grusdt, C. Repellin, N. Goldman, and M. Greiner, Realization of a fractional quantum hall state with ultracold atoms, *Nature* **619**, 495 (2023).
- [18] N. Gemelke, E. Sarajlic, and S. Chu, *Rotating few-body atomic systems in the fractional quantum hall regime* (2010), [arXiv:1007.2677 \[cond-mat.quant-gas\]](https://arxiv.org/abs/1007.2677).
- [19] P. Lunt, P. Hill, J. Reiter, P. M. Preiss, M. Gałka, and S. Jochim, Realization of a Laughlin state of two rapidly rotating fermions, [arXiv:2402.14814](https://arxiv.org/abs/2402.14814) (2024).
- [20] L. W. Clark, N. Schine, C. Baum, N. Jia, and J. Simon, Observation of Laughlin states made of light, *Nature* **582**, 41 (2020).
- [21] C. Wang, F.-M. Liu, M.-C. Chen, H. Chen, X.-H. Zhao, C. Ying, Z.-X. Shang, J.-W. Wang, Y.-H. Huo, C.-Z. Peng, *et al.*, Realization of fractional quantum hall state with interacting photons, *Science* **384**, 579 (2024).
- [22] T. Blatz, J. Kwan, J. Léonard, and A. Bohrdt, Bayesian optimization for robust state preparation in quantum many-body systems, *Quantum* **8**, 1388 (2024).
- [23] N. Khaneja, T. Reiss, C. Kehlet, T. Schulte-Herbrüggen, and S. J. Glaser, Optimal control of coupled spin dynamics: design of nmr pulse sequences by gradient as-



- cent algorithms, *Journal of Magnetic Resonance* **172**, 296 (2005).
- [24] S. van Frank, M. Bonneau, J. Schmiedmayer, S. Hild, C. Gross, M. Cheneau, I. Bloch, T. Pichler, A. Negretti, T. Calarco, and S. Montangero, Optimal control of complex atomic quantum systems, *Scientific Reports* **6**, 34187 (2016).
- [25] X. Li, D. Pecak, T. Sowiński, J. Sherson, and A. E. B. Nielsen, Global optimization for quantum dynamics of few-fermion systems, *Phys. Rev. A* **97**, 033602 (2018).
- [26] S. E. Sklarz and D. J. Tannor, Loading a bose-einstein condensate onto an optical lattice: An application of optimal control theory to the nonlinear schrödinger equation, *Phys. Rev. A* **66**, 053619 (2002).
- [27] P. Doria, T. Calarco, and S. Montangero, Optimal control technique for many-body quantum dynamics, *Phys. Rev. Lett.* **106**, 190501 (2011).
- [28] J. J. W. H. Sørensen, M. O. Aramburu, T. Heinzel, and J. F. Sherson, Quantum optimal control in a chopped basis: Applications in control of bose-einstein condensates, *Phys. Rev. A* **98**, 022119 (2018).
- [29] S. Machnes, E. Assémat, D. Tannor, and F. K. Wilhelm, Tunable, flexible, and efficient optimization of control pulses for practical qubits, *Phys. Rev. Lett.* **120**, 150401 (2018).
- [30] R. Storn and K. Price, Differential evolution – a simple and efficient heuristic for global optimization over continuous spaces, *Journal of Global Optimization* **11**, 341 (1997).
- [31] N. Hansen, The cma evolution strategy: A comparing review, in *Towards a New Evolutionary Computation: Advances in the Estimation of Distribution Algorithms*, edited by J. A. Lozano, P. Larrañaga, I. Inza, and E. Bengoetxea (Springer Berlin Heidelberg, Berlin, Heidelberg, 2006) pp. 75–102.
- [32] S. Lloyd and S. Montangero, Information theoretical analysis of quantum optimal control, *Phys. Rev. Lett.* **113**, 010502 (2014).
- [33] D. D’Alessandro and M. Dahleh, Optimal control of two-level quantum systems, *IEEE Transactions on Automatic Control* **46**, 866 (2001).
- [34] U. Boscain, G. Charlot, J.-P. Gauthier, S. Guérin, and H.-R. Jauslin, Optimal control in laser-induced population transfer for two- and three-level quantum systems, *Journal of Mathematical Physics* **43**, 2107 (2002), <https://aip.scitation.org/doi/pdf/10.1063/1.1465516>.
- [35] N. Khaneja, R. Brockett, and S. J. Glaser, Time optimal control in spin systems, *Phys. Rev. A* **63**, 032308 (2001).
- [36] U. Boscain and Y. Chitour, Time-optimal synthesis for left-invariant control systems on  $so(3)$ , *SIAM Journal on Control and Optimization* **44**, 111 (2005), <https://doi.org/10.1137/S0363012904441532>.
- [37] U. Boscain and P. Mason, Time minimal trajectories for a spin 1/2 particle in a magnetic field, *Journal of Mathematical Physics* **47**, 062101 (2006), <https://doi.org/10.1063/1.2203236>.
- [38] U. Boscain, F. Grönberg, R. Long, and H. Rabitz, Minimal time trajectories for two-level quantum systems with two bounded controls, *Journal of Mathematical Physics* **55**, 062106 (2014), <https://doi.org/10.1063/1.4882158>.
- [39] G. C. Hegerfeldt, Driving at the quantum speed limit: Optimal control of a two-level system, *Phys. Rev. Lett.* **111**, 260501 (2013).
- [40] G. C. Hegerfeldt, High-speed driving of a two-level system, *Phys. Rev. A* **90**, 032110 (2014).
- [41] A. D. Boozer, Time-optimal synthesis of  $su(2)$  transformations for a spin-1/2 system, *Phys. Rev. A* **85**, 012317 (2012).
- [42] M. Jafarizadeh, F. Naghdi, and M. Bazrafkan, Time optimal control of two-level quantum systems, *Physics Letters A* **384**, 126743 (2020).
- [43] P. G. Harper, General motion of conduction electrons in a uniform magnetic field, *Proceedings of the Physical Society. Section A* **68**, 879 (1955).
- [44] D. R. Hofstadter, Energy levels and wave functions of bloch electrons in rational and irrational magnetic fields, *Physical Review B* **14**, 2239 (1976).
- [45] A. S. Sørensen, E. Demler, and M. D. Lukin, Fractional quantum Hall states of atoms in optical lattices, *Phys. Rev. Lett.* **94**, 086803 (2005).
- [46] D. N. Sheng, Z.-C. Gu, K. Sun, and L. Sheng, Fractional quantum hall effect in the absence of landau levels, *Nat. Commun.* **2**, 389 (2011).
- [47] T. Neupert, L. Santos, C. Chamon, and C. Mudry, Fractional quantum Hall states at zero magnetic field, *Phys. Rev. Lett.* **106**, 236804 (2011).
- [48] N. Regnault and B. A. Bernevig, Fractional Chern insulator, *Phys. Rev. X* **1**, 021014 (2011).
- [49] Z. Liu and E. J. Bergholtz, Recent developments in fractional chern insulators, in *Encyclopedia of Condensed Matter Physics (Second Edition)*, edited by T. Chakraborty (Academic Press, Oxford, 2024) second edition ed., pp. 515–538.
- [50] R. N. Palmer and D. Jaksch, High-field fractional quantum Hall effect in optical lattices, *Phys. Rev. Lett.* **96**, 180407 (2006).
- [51] M. Hafezi, A. S. Sørensen, E. Demler, and M. D. Lukin, Fractional quantum Hall effect in optical lattices, *Phys. Rev. A* **76**, 023613 (2007).
- [52] M. Gerster, M. Rizzi, P. Silvi, M. Dalmonte, and S. Montangero, Fractional quantum Hall effect in the interacting Hofstadter model via tensor networks, *Phys. Rev. B* **96**, 195123 (2017).
- [53] P. Rosson, M. Lubasch, M. Kiffner, and D. Jaksch, Bosonic fractional quantum Hall states on a finite cylinder, *Phys. Rev. A* **99**, 033603 (2019).
- [54] X.-Y. Dong, A. G. Grushin, J. Motruk, and F. Pollmann, Charge excitation dynamics in bosonic fractional Chern insulators, *Phys. Rev. Lett.* **121**, 086401 (2018).
- [55] M. Račiūnas, F. N. Ünal, E. Anisimovas, and A. Eckardt, Creating, probing, and manipulating fractionally charged excitations of fractional Chern insulators in optical lattices, *Phys. Rev. A* **98**, 063621 (2018).
- [56] E. Macaluso, T. Comparin, R. O. Umucalılar, M. Gerster, S. Montangero, M. Rizzi, and I. Carusotto, Charge and statistics of lattice quasiholes from density measurements: A tree tensor network study, *Phys. Rev. Research* **2**, 013145 (2020).
- [57] J. Motruk and I. Na, Detecting fractional Chern insulators in optical lattices through quantized displacement, *Phys. Rev. Lett.* **125**, 236401 (2020).
- [58] C. Repellin, J. Léonard, and N. Goldman, Fractional Chern insulators of few bosons in a box: Hall plateaus from center-of-mass drifts and density profiles, *Phys. Rev. A* **102**, 063316 (2020).
- [59] J. A. Kjäll and J. E. Moore, Edge excitations of bosonic fractional quantum Hall phases in optical lattices, *Phys.*

- Rev. B **85**, 235137 (2012).
- [60] C. Repellin and N. Goldman, Detecting fractional Chern insulators through circular dichroism, *Phys. Rev. Lett.* **122**, 166801 (2019).
- [61] F. A. Palm, S. Mardazad, A. Bohrdt, U. Schollwöck, and F. Grusdt, Snapshot-based detection of  $\nu = \frac{1}{2}$  Laughlin states: Coupled chains and central charge, *Phys. Rev. B* **106**, L081108 (2022).
- [62] H. Dehghani, Z.-P. Cian, M. Hafezi, and M. Barkeshli, Extraction of the many-body Chern number from a single wave function, *Phys. Rev. B* **103**, 075102 (2021).
- [63] Z.-P. Cian, H. Dehghani, A. Elben, B. Vermersch, G. Zhu, M. Barkeshli, P. Zoller, and M. Hafezi, Many-body Chern number from statistical correlations of randomized measurements, *Phys. Rev. Lett.* **126**, 050501 (2021).
- [64] B. Wang, X.-Y. Dong, and A. Eckardt, Measurable signatures of bosonic fractional Chern insulator states and their fractional excitations in a quantum-gas microscope, *SciPost Phys.* **12**, 095 (2022).
- [65] J. Boesl, R. Dilip, F. Pollmann, and M. Knap, Characterizing fractional topological phases of lattice bosons near the first mott lobe, *Phys. Rev. B* **105**, 075135 (2022).
- [66] Q. Niu, D. J. Thouless, and Y.-S. Wu, Quantized hall conductance as a topological invariant, *Phys. Rev. B* **31**, 3372 (1985).
- [67] R. Tao and F. D. M. Haldane, Impurity effect, degeneracy, and topological invariant in the quantum hall effect, *Phys. Rev. B* **33**, 3844 (1986).
- [68] M. Popp, B. Paredes, and J. I. Cirac, Adiabatic path to fractional quantum Hall states of a few bosonic atoms, *Phys. Rev. A* **70**, 053612 (2004).
- [69] N. R. Cooper and J. Dalibard, Reaching fractional quantum Hall states with optical flux lattices, *Phys. Rev. Lett.* **110**, 185301 (2013).
- [70] N. Y. Yao, A. V. Gorshkov, C. R. Laumann, A. M. Läuchli, J. Ye, and M. D. Lukin, Realizing fractional Chern insulators in dipolar spin systems, *Phys. Rev. Lett.* **110**, 185302 (2013).
- [71] E. Kapit, M. Hafezi, and S. H. Simon, Induced self-stabilization in fractional quantum Hall states of light, *Phys. Rev. X* **4**, 031039 (2014).
- [72] F. Grusdt, F. Letscher, M. Hafezi, and M. Fleischhauer, Topological growing of Laughlin states in synthetic gauge fields, *Phys. Rev. Lett.* **113**, 155301 (2014).
- [73] M. Barkeshli, N. Y. Yao, and C. R. Laumann, Continuous preparation of a fractional Chern insulator, *Phys. Rev. Lett.* **115**, 026802 (2015).
- [74] C. Repellin, T. Yefsah, and A. Sterdyniak, Creating a bosonic fractional quantum Hall state by pairing fermions, *Phys. Rev. B* **96**, 161111 (2017).
- [75] J. Motruk and F. Pollmann, Phase transitions and adiabatic preparation of a fractional Chern insulator in a boson cold-atom model, *Phys. Rev. B* **96**, 165107 (2017).
- [76] Y.-C. He, F. Grusdt, A. Kaufman, M. Greiner, and A. Vishwanath, Realizing and adiabatically preparing bosonic integer and fractional quantum Hall states in optical lattices, *Phys. Rev. B* **96**, 201103 (2017).
- [77] A. Hudomal, N. Regnault, and I. Vasić, Bosonic fractional quantum Hall states in driven optical lattices, *Phys. Rev. A* **100**, 053624 (2019).
- [78] B. Andrade, V. Kasper, M. Lewenstein, C. Weitenberg, and T. Graß, Preparation of the  $1/2$  Laughlin state with atoms in a rotating trap, *Phys. Rev. A* **103**, 063325 (2021).
- [79] F. A. Palm, J. Kwan, B. Bakkali-Hassani, M. Greiner, U. Schollwöck, N. Goldman, and F. Grusdt, Growing extended Laughlin states in a quantum gas microscope: A patchwork construction, *Phys. Rev. Res.* **6**, 013198 (2024).
- [80] B. Wang, M. Aidelsburger, J. Dalibard, A. Eckardt, and N. Goldman, Cold-atom elevator: From edge-state injection to the preparation of fractional Chern insulators, *Phys. Rev. Lett.* **132**, 163402 (2024).
- [81] N. Hansen, Y. Akimoto, and P. Baudis, [CMA-ES/pycma on Github](#), Zenodo, DOI:10.5281/zenodo.2559634 (2019).
- [82] C. Sträter and A. Eckardt, Interband heating processes in a periodically driven optical lattice, *Zeitschrift für Naturforschung A* **71**, 909 (2016).
- [83] A. Widom, Thermodynamic derivation of the hall effect current, *Physics Letters A* **90**, 474 (1982).
- [84] P. Streda, Theory of quantised hall conductivity in two dimensions, *Journal of Physics C: Solid State Physics* **15**, L717 (1982).
- [85] P. Streda and L. Smrcka, Thermodynamic derivation of the hall current and the thermopower in quantising magnetic field, *Journal of Physics C: Solid State Physics* **16**, L895 (1983).
- [86] R. O. Umucalılar, H. Zhai, and M. O. Oktel, Trapped fermi gases in rotating optical lattices: Realization and detection of the topological Hofstadter insulator, *Phys. Rev. Lett.* **100**, 070402 (2008).
- [87] G. Sun and A. Eckardt, Optimal frequency window for Floquet engineering in optical lattices, *Phys. Rev. Res.* **2**, 013241 (2020).

## Appendix A: CMA-ES

CMA-ES (Covariance Matrix Adaptation Evolution Strategy) [31] is an advanced evolutionary algorithm for optimizing complex problems. It operates on a population of candidate solutions, evolving them through a process that mimics natural selection. The key innovation of CMA-ES is its ability to adaptively adjust the covariance matrix of the population's distribution, allowing it to efficiently explore and exploit the search space without requiring gradient information. This makes CMA-ES particularly effective for non-linear, non-convex, and multi-modal optimization problems.

Here is a detailed explanation of CMA-ES mechanism:

- 1. Initialization:** Start with an initial population of candidate solutions, represented by a mean vector  $\mathbf{x}_{\text{mean}}$  and a covariance matrix  $\mathbf{C}$ . Set an initial step size  $\sigma$  and define parameters like the population size  $\lambda$  and the number of selected parents  $\mu$ .
- 2. Sampling New Solutions:** Generate a new population of  $\lambda$  candidate solutions by sampling from a multivariate normal distribution defined by the current  $\mathbf{x}_{\text{mean}}$  and  $\mathbf{C}$ . This is done by first sampling standard normal vectors  $\mathbf{z}$  and then transforming them using the covariance matrix:  $\mathbf{x} =$

$\mathbf{x}_{\text{mean}} + \sigma \mathbf{B} \mathbf{D} \mathbf{z}$ , where  $\mathbf{B}$  and  $\mathbf{D}$  are derived from the eigendecomposition of  $\mathbf{C}$ .

3. **Evaluation:** Evaluate the fitness of each new solution using the objective function. The fitness values guide the selection of the best solutions for the next generation.
4. **Selection:** Select the top  $\mu$  solutions based on their fitness to form the parents for the next generation. This selection process is crucial for maintaining diversity and guiding the search towards better solutions.
5. **Updating the Mean:** Update the mean vector  $\mathbf{x}_{\text{mean}}$  by calculating a weighted sum of the selected parents. The weights are determined by their fitness, with better solutions contributing more to the new mean.
6. **Covariance Matrix Adaptation:** Adapt the covariance matrix  $\mathbf{C}$  to better model the distribution of the selected solutions. This involves updating the matrix based on the differences between the selected solutions and the current mean. Two main updates are performed: a rank-one update that captures the direction of the best solutions, and a rank- $\mu$  update that considers the spread of the selected solutions.
7. **Step Size Control:** Adjust the step size  $\sigma$  based on the success of the search. A larger step size allows for more exploration, while a smaller step size enables finer exploitation of promising areas.
8. **Termination:** Continue the iterations until a stopping criterion is met, such as reaching a maximum number of evaluations or finding a solution with a fitness below a certain threshold.
9. **Output:** Return the best solution found during the search process.

CMA-ES's effectiveness stems from its ability to balance exploration (through the covariance matrix and step size adaptation) and exploitation (through selection and mean update), making it a robust choice for a wide range of optimization tasks.

## Appendix B: GRAPE for Harvard experiment

To benchmark the results obtained using smooth control protocol, We employ GRAdient Ascend Pulse Engineering (GRAPE) [23] method to optimize piecewise constant control fields, for the  $4 \times 4$  lattice system. The four-step-ramping protocol is as follows:

In step 1, we take  $T_1 = 6\tau$  to linearly increase the tunneling  $t_y$  from 0 to  $\hbar/\tau$ . In step 2 the minimal duration is estimated  $T_2 = 4\tau$ , as well as the optimized control field  $\Delta_y(t)$  by using GRAPE (see left panel of Fig. 11). At

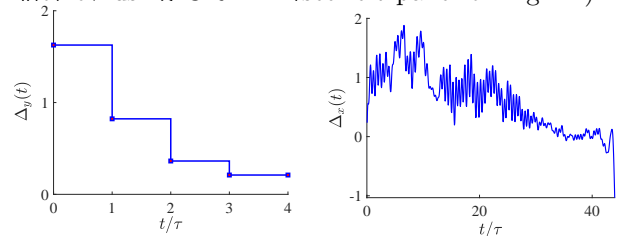


FIG. 11. Control fields  $\Delta_y(t)$  and  $\Delta_x(t)$  optimized using GRAPE. Left: Optimized control field  $\Delta_y(t)$  in step 2 in scheme 1. A nearly perfect fidelity  $F = 99.3\%$  is obtained with a short duration  $T_2 = 4\tau$ . Right: Optimized control field  $\Delta_x(t)$  in step 4. A nearly perfect fidelity  $F = 99.1\%$ , with the Laughlin-type FQHE state, is obtained with duration  $T_4 = 44\tau$ .

the end of step 2, the two particles are delocalized into one column. The final state of time evolution in step 2 is the initial state of step 3.

In step 3, we linearly increase the tunneling strength  $t_x$  from 0 to  $\hbar/\tau$  over time  $T_3 = 5\tau$ . In step 4, a high fidelity  $F = 99.1\%$  is obtained with a duration  $T_4 = 44\tau$  using GRAPE (see right panel of Fig. 11). The total duration of state preparation is  $T = \sum_{n=1}^4 T_n = 59\tau$ , which is a bit longer than the minimal duration  $T = 54\tau$  using smooth control protocol (refer to Sec. III A).

We notice that the optimized control field  $\Delta_x(t)$  obtained with GRAPE oscillates rapidly (see right panel of Fig. 11). This makes such control protocols less favorable in experiments. Such an issue could be resolved by adding a penalty function which penalizes rapidly fluctuating controls. However, it usually makes the optimization more complicated, and the minimal duration to reach the target state is in general longer than the one without penalty function. Therefore, we stick to the smooth function, as illustrated in the main text.